Ultramicroscopy 285 (2026) 114409

Contents lists available at ScienceDirect

Ultramicroscopy

journal homepage: www.elsevier.com/locate/ultramic

Temperature-dependent mean inner potential of polystyrene spheres measured using off-axis electron holography

Yan Lu [a,*], Peng-Han Lu [a], Fengshan Zheng [a,b], Dominik Biscette [c], Denys Sutter [c], Johan Chang [c], Giulio Pozzi [a,d], Rafal E. Dunin-Borkowski [a]

[a] Ernst Ruska-Centre for Microscopy and Spectroscopy with Electrons, Forschungszentrum Jülich GmbH, 52428 Jülich, Germany
[b] Spin-X Institute, Electron Microscopy Center, School of Physics and Optoelectronics, State Key Laboratory of Luminescent Materials and Devices, Guangdong-Hong Kong-Macao Joint Laboratory of Optoelectronic and Magnetic Functional Materials, South China University of Technology, Guangzhou, China
[c] condenZero AG, 8050 Zürich, Switzerland
[d] Department FIM, University of Modena and Reggio Emilia, via G. Campi 213/a, 41125 Modena, Italy

ARTICLE INFO

Keywords:
Off-axis electron holography
Electrostatic potential
Mean inner potential
Electron-beam-induced charge
Liquid helium

ABSTRACT

Off-axis electron holography is used to measure the temperature dependence of the mean inner potential and electron-beam-induced charging effects in polystyrene spheres with diameters of between 230 and 600 nm from room temperature to 5.3 K. Integrating the model independent and line fitting simulation approaches, enabled by the high quality of the recorded holograms, it has been possible to disentangle the contribution the beam induced charge from that of the mean inner potential (MIP), finding that both quantities (at least for the smaller spheres) increase with decreasing temperature. In particular the MIP reaches a value of (6.48 ± 0.24) V at 5.3 K, corresponding to an increase of 16.8% ± 4.2%, with respect to the measurements carried at room temperature, giving the value (5.55 ± 0.07) V.

1. Introduction

The mean inner potential (MIP) is the volume-averaged electrostatic potential of a material relative to a zero of potential at an infinite distance in vacuum. It is an important property for the quantitative interpretation of measurements recorded using phase contrast techniques in the transmission electron microscope (TEM), such as electron holography and electron ptychography, in which an incident electron wave starts at a large distance from the sample before passing through it [1,2]. Estimates of MIPs, which date back to the work of Bethe [3], have been based on calculations of electron scattering factors [4], analytical calculations combining nuclear and electronic cloud potentials [5], density functional theory simulations [6,7], *ab initio* studies [8,9] and molecular modeling [10,11] for both crystalline and amorphous materials.

Electron holography is a powerful technique for measuring the phase shift of an electron wave that has passed through a sample in the TEM. In-line electron holography was originally proposed by Gabor [12], with the reference and object wave sharing the same optical axis. In off-axis electron holography, the reference wave that has passed through vacuum and the object wave that has passed through the region of interest on the sample can be separated and interfered by applying a voltage to a biprism filament [13]. The recorded hologram can be used to reconstruct both amplitude and phase information about the sample. An additional empty reference hologram (with the sample removed from the field of view) is typically used to compensate the distortion-induced phase modulations by subtracting it. A Fourier-transform-based method is usually used to reconstruct each hologram to obtain amplitude and phase information [14]. The technique is now frequently used for mapping electromagnetic fields, with improved phase sensitivity achieved by using coherent elliptical illumination [15–18].

In the absence of dynamical diffraction effects and magnetic fields, the recorded phase shift can be expressed in the form

$$\varphi(x,y) = C_{\mathrm{E}} \int_{-\infty}^{+\infty} V_{\mathrm{t}}(x,y,z)\,dz, \tag{1}$$

where z is the incident electron beam direction, x and y are coordinates in the sample plane, V_{t} is the total potential, including the MIP, contributions to the potential resulting from charge redistribution in the sample and the electrostatic potential above and below the sphere in the vacuum. C_{E} is a constant that is dependent on the microscope accelerating voltage in the form of $(2\pi e/\lambda)(E+E_0)/(E(E+2E_0))$ where λ is wavelength of electron beam, E is the energy and E_0 is the rest mass energy of the electron [14]; it takes a value of 6.52×10^6 rad/(Vm)

* Corresponding author.
E-mail address: y.lu@fz-juelich.de (Y. Lu).

https://doi.org/10.1016/j.ultramic.2026.114409
Received 15 February 2026; Received in revised form 4 June 2026; Accepted 11 June 2026
Available online 16 June 2026

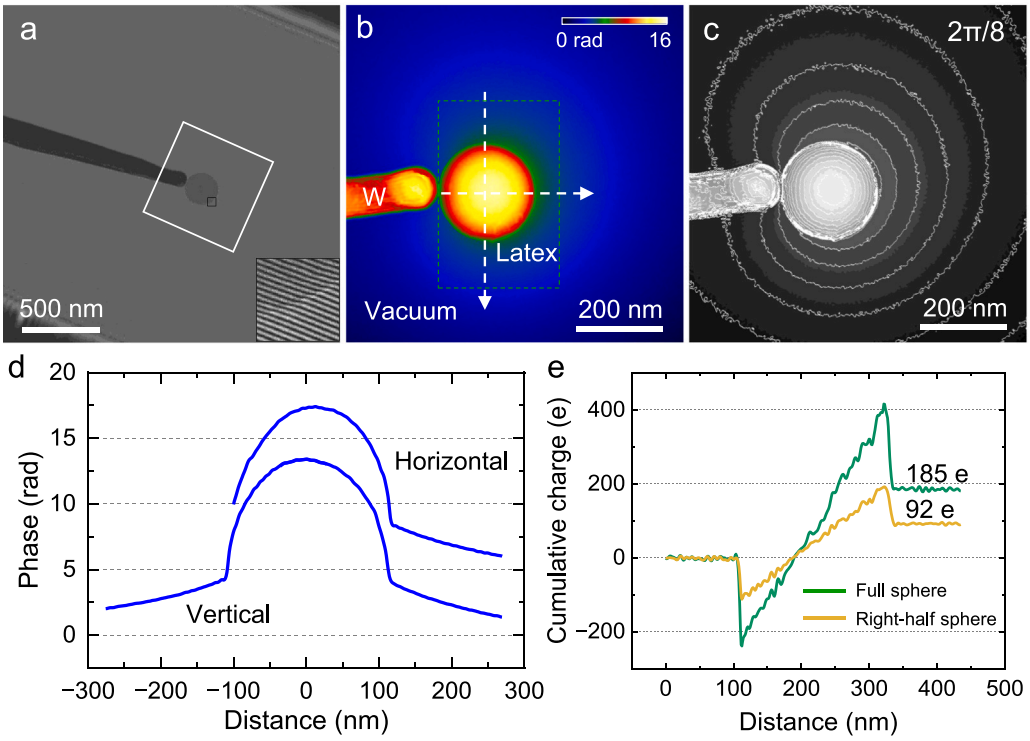

Fig. 1. Electron-beam-inducted charging at RT using off-axis electron holography. (a) Low magnification view of a representative off-axis electron hologram of a polystyrene sphere of diameter 226 nm attached to the tip of a tungsten needle recorded at room temperature. The extent of the overlap region is visible at the upper right and lower left corners. The white box marks the region used for final hologram acquisition, reconstruction and analysis. The lower right inset shows the magnified interference fringes of the area in the black box. (b) Unwrapped phase image. The horizontal and vertical white dashed arrows mark the positions used to generate phase profiles. The green dashed frame, which includes the full extent of the polystyrene sphere, marks the extent of the loop integral used for cumulative charge measurement using the MI approach. (c) Equiphase contour lines of spacing $2\pi/8$ rad superimposed on the phase image. (d) Phase profiles (offset vertically for clarity) extracted at the positions of the dashed arrows in (b). (e) Cumulative charge profiles of the full sphere (green line) and the right-half sphere (yellow line), providing values for the total charge in each region of 185 and 92 e, respectively.

at 300 kV. The contribution to the total potential from the MIP is contained within the material and does not decay significantly into the vacuum surrounding it.

Off-axis electron holography has been used to measure the MIPs of semiconductors [6,19], metal particles [20], two-dimensional materials [21,22], liquid water [23] and amorphous particles and films [24–27]. Such measurements are typically made by plotting the measured phase shift as a function of sample thickness. The MIP is obtained from the slope of the resulting linear dependence of phase shift on thickness (especially for amorphous and weakly diffracting crystalline specimens).

Here, we use off-axis electron holography to measure values of MIP of polystyrene spheres with diameters of between 200 and 600 nm at temperatures of between room temperature (RT) and 5.3 K, while taking into account and quantifying the effects of electron-beam-induced charging using both Laplacian-based methods [28–30] and analytical methods [24,26,30,31]. In addition to the separation of the induced charge and MIP effects, an increase of the MIP with decreasing temperature, based on a statistical analysis of more than 20 measurements of spheres of different size, has been observed.

2. Methods

2.1. Sample

The polystyrene spheres with different sizes were purchased from Merck KGaA, suspended in a 0.1% sodium azide solution. They are atactic type, which means the phenyl groups, (C_6H_5) in the formula $[-CH_2-CH(C_6H_5)-]_n$, are arranged randomly on both sides of the polymer chain, showing an amorphous structure, comparing to semi-crystal syndiotatic (phenyl groups arranged alternatively alongside the chain) and semi-crystal isotatic (phenyl groups arranged at same side of the chain). This amorphous atatic structure prevents crystallization even at low temperature [32].

The original suspension was highly diluted with distilled water and subsequently dispersed by ultrasonication. TEM sample was prepared by depositing 3 to 5 drops onto a TEM grid, followed by complete air-drying. The grid was then immediately loaded into TEM for observation.

2.2. Off-axis electron holography

Off-axis electron holograms were recorded at 300 kV using an FEI Titan G2 TEM equipped with a 4K Gatan K2 camera. A Lorentz lens and a biprism placed above the selected area lens were used to obtain large fields of view. A biprism voltage of 110 V was used, corresponding to a holographic interference fringe spacing of 2.59 nm and a field of view of approximately 2 μm with reference to the sample plane. Selected polystyrene spheres were placed in the center of the field of view, in order to avoid effects on the reconstructed amplitude and phase of Fresnel fringes from the edges of the biprism (as shown in Fig. 1a). Elliptical illumination was used to maximize the contrast of the holographic interference fringes. Image astigmatism was corrected after selecting the desired elliptical illumination and electron biprism bias voltage. Close to RT, each hologram was acquired with an exposure time of 6 s at a dose rate of 1 to 2 e/(Å^{2}s). At lower sample temperature, 30 frames at 0.2 s per frame were recorded while maintaining the same dose rate. Individual frames that exhibited significant blurring were removed before reconstruction. Hologram reconstruction was performed

using HoloWorks software, including subtraction of phase images obtained from empty (vacuum) reference holograms and averaged of reconstructed complex images for stacking data [33].

The magnification was carefully calibrated before data collection using a cross-grating grid with a line pitch spacing of 463 nm in both orthogonal directions. The actual magnification and pixel size of each image are recorded in Gatan GMS software, and they will be shown correspondingly for each experimental figure in this manuscript. Comparison of these parameters confirmed that the magnification calibration of all holograms was consistent.

Fig. 1a shows a representative off-axis electron hologram, recorded at RT, of a polystyrene sphere with a diameter of 226 nm attached to the end of an electrochemically etched W needle in a NanoFactory specimen holder, with the acquisition area marked by a white frame. The W needle is connected to the ground. The lower right inset shows magnified holographic interference fringes at the boundary between the polystyrene sphere and vacuum of the black box. From the inset, it is clearly observed that the interference fringes shift while crossing the boundary, while each fringe maintains continuity. The intensity of the hologram includes amplitude and phase in a complex form. In order to reconstruct the phase that comprises electrostatic potential, a Fourier transform is applied to the hologram, followed by an inverse Fourier transform of one of the two sidebands [14]. The phase signs of two sidebands are opposite, and all the reconstruction was processed by choosing the sideband which contains positive phase.

Figs. 1b and c show a reconstructed phase image and corresponding equiphase contours of spacing $2\pi/8$ rad, respectively. The recorded object and reference holograms are at actual magnification of 18 300× and pixel size of 0.2727 nm. Phase profiles extracted along the dashed vertical and horizontal arrows are shown in Fig. 1d. The projected electrostatic potential in the polystyrene sphere contains contributions from the MIP of the sphere and from the effect of electron-beam-induced charging. In contrast, the equiphase contours in vacuum surrounding the polystyrene sphere are associated with electron-beam-induced charging alone. The directions of the equiphase contours that cross the W tip suggest that it is oppositely charged to the polystyrene sphere. The asymmetry of the contours in vacuum with respect to the axis of symmetry of the needle and the sphere results primarily from perturbation of the reference wave [34], which is not flat but includes the projected potential associated with the long-range electrostatic field of the charge on the sphere. This contribution to the potential is then included with an opposite sign in the recorded phase image. The corresponding phase profile in vertical direction shown in Fig. 1d displays this asymmetry in the vacuum regions above and below the sphere. The perturbation is equivalent to the presence of an oppositely charged sphere in the lower region and results in a higher density of the contours below the sphere than above it. The treatment of this perturbation in simulation is addressed in Section 2.5.

Reduced sample temperatures were reached by using a condenZero liquid-helium-cooled specimen holder (between 5 and 77 K) and a Gatan liquid-nitrogen-cooled specimen holder (between 98 K and RT). The temperature in the condenZero specimen holder is measured closely adjacent to the sample.

2.3. Electron optical phase simulation

For a spherical solid object of radius R, the projected phase shift contributed by the MIP, φ_{MIP}, depends on x and y because of the change in sample thickness (in the z direction), taking the form

$$\varphi_{\mathrm{MIP}}(x,y) = 2C_{\mathrm{E}}V_{\mathrm{MIP}}(x,y)\sqrt{R^2-(x^2+y^2)} \tag{2}$$

when $r \le R$, i.e., $\sqrt{x^2+y^2+z^2} \le R$ (see details in the Supplementary Material).

The decay in phase from the polystyrene sphere surface into the vacuum region results from the presence of a three-dimensional electric field generated by the charge on the polystyrene sphere. The difference between surface charge and volume charge contributions to cumulative charge and phase profiles can be found in Supplementary Material. For a uniformly-charged sphere at position (0, 0, 0) with total charge Q and a compensating charge $-Q$ at (x_0, y_0, 0), ensuring overall charge neutrality, the contribution φ_{Q} to the phase shift at point (r) from the charge can be written in the following forms (see derivation details in Supplementary Material).

If $r \ge R$ [31]:

$$\varphi_{\mathrm{Q}}(x,y) = C_{\mathrm{E}}\frac{Q}{4\pi\epsilon_0}\ln\frac{(x-x_0)^2+(y-y_0)^2}{x^2+y^2}, \tag{3}$$

where ϵ_0 is the vacuum permittivity.

If $0 \le r < R$:

$$\varphi_{\mathrm{Q}}(x,y) = 2C_{\mathrm{E}}\frac{Q}{4\pi\epsilon_0}\left(\ln\frac{\sqrt{(x-x_0)^2+(y-y_0)^2}}{\sqrt{R^2-x^2-y^2}+R} + \frac{\sqrt{R^2-x^2-y^2}}{R}\right). \tag{4}$$

Note that the position of the compensating charge is outside of the field of view, so that $x - x_0 \neq 0$ and $y - y_0 \neq 0$.

The total projected phase shift $\varphi(x,y)$ can then be written in the form

$$\varphi(x,y) = \varphi_{\mathrm{MIP}}(x,y) + \varphi_{\mathrm{Q}}(x,y). \tag{5}$$

The phase in the field of view is given by Eqs. (3),innerphase, highlighting the advantage of using a compensating point charge instead of a large concentric sphere [24] to achieve charge neutrality.

2.4. Quantification of charge

Of the different methods that can be used to quantitatively measure the charge on a polystyrene sphere from a phase image, a model-independent (MI) approach [28–30] is particularly valuable for calculating total charge within a selected region of the image based on classical electromagnetic principles. The electrostatic potential generated by a charge distribution $\rho(x,y,z)$ follows the Poisson equation

$$\nabla^2 V_{\mathrm{t}}(x,y,z) = -\frac{\rho(x,y,z)}{\epsilon_0}. \tag{6}$$

By substituting Eq. (6) into Eq. (1), the relation between the projected phase shift and the projected charge density $\sigma(x,y)$ takes the form

$$\nabla^2\varphi(x,y) = -C_{\mathrm{E}}\frac{\sigma(x,y)}{\epsilon_0}, \tag{7}$$

showing that the Laplacian of the phase shift is proportional to the projected charge density. The charge Q is then the integral of the projected charge density in the x and y directions and the relation between the amount of charge and the projected phase shift can be written in the form

$$Q = \iint \sigma(x,y)dxdy = -\frac{\epsilon_0}{C_{\mathrm{E}}}\iint \nabla^2\varphi(x,y)dxdy, \tag{8}$$

showing that the amount of charge is proportional to the double integral of the Laplacian of the phase over a selected region. Furthermore, the double integral of a projected surface charge density over a closed integration path is equal to the contour integral of the gradient, while the Laplacian operator is the divergence of the gradient (the second partial derivative of the projected surface charge density). The amount of charge in a region with outward normal $\vec{N}$ and line parameter s in the projected phase shift can then also take the form

$$Q = -\frac{\epsilon_0}{C_{\mathrm{E}}}\oint \nabla\varphi(x(s),y(s))\cdot\vec{N}(x(s),y(s))ds. \tag{9}$$

After applying Eq. (9) to the phase shift image shown in Fig. 1b, Fig. 1e shows the cumulative charge calculated for both the full sphere and the right half of the sphere. The full sphere contains twice the charge of the half sphere. The steps in the curves at ~100 and ~320 nm are due to effective surface charge dipoles contributed by the MIP. The positive charge is induced by the secondary electron emission while electron beam irradiates on the sample [35]. The charge on polystyrene

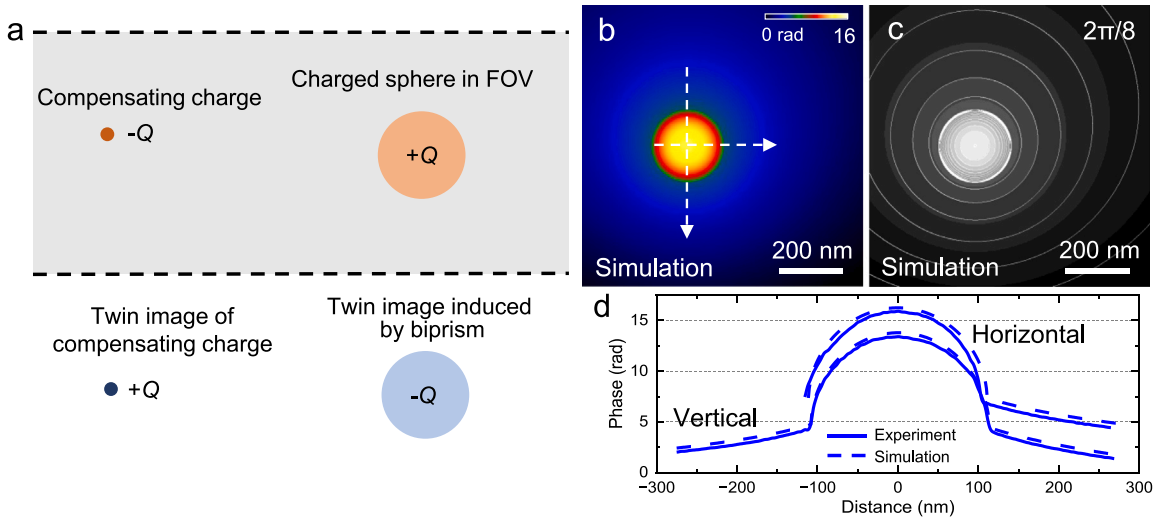

Fig. 2. Determination of charge amount and MIP using analytical method. (a) Schematic diagram of original charged sphere (orange patterns) and the twin image induced by biprism (blue patterns). The gray area is the field of view of interference hologram. The dashed lines indicate the direction of biprism. The charge from twin image is considered as an opposite charge placed in a direction perpendicular to the biprism. Here, the compensating charge is distant from the original charge, and it ensures overall charge neutrality. (b) Simulated phase shift for a total charge of 140 e and a MIP of 5.50 V. The intensity scale is normalized to the same range as for the experimental phase image. (c) Corresponding equiphase contour lines of spacing $2\pi/8$ rad. (d) Comparison between phase profiles (offset vertically for clarity) extracted at the same positions from the experimental (solid lines) and simulated (dashed lines) phase images.

spheres could not transfer to the conductive support materials due to the Schottky barrier on metal and polymer interface [36]. The cumulative charge on the sphere increases linearly, suggesting that it is distributed homogeneously on its surface [30] (see details in Supplementary Material), with minimal boundary effects from the W tip.

2.5. Quantification of MIP

The MIP and electron-beam-induced charging contributions to the phase can be disentangled by recognizing that line profiles of the phase from the vacuum region into the center of the particle can be fitted accurately using the equations in Section 2.3 due to the high signal-to-noise ratio of phase profile, even if the entire two-dimensional map is perturbed by charge in the supporting material and by the twin image introduced by recording the hologram.

It is important to note that none of these perturbing effects influence the MI approach, which is only sensitive to the charge in the selected integration region. By combining these two approaches in a self-consistent manner, it is possible to obtain a more accurate value of the MIP, when compared with an approach that overlooks the charge in the particle. As a test of the method, we consider its application to the experimental results shown in Fig. 1.

Fig. 1c presents the asymmetry in the phase decay, which results from factors such as the charge on the W tip, possible charge on the sample holder and sample grid, and the perturbed reference wave (PRW). The effect on the phase in the field of view (FOV) of the PRW is shown in Fig. 2a , where the direction of biprism is same as the dashed lines. The electrostatic potential of the charged sphere decays from the surface to the edge of the FOV and further spreads in the reference wave. The PRW contributes to the recorded hologram when interfering with the objective wave. This contribution is equivalent to that of a point charge $-Q$ at the position $(0, D, 0)$, where D is the FOV width (2 μm in this study) [34,37], as shown in Fig. 2a. In addition to the charged sphere in the FOV, it is also shown the compensating charge $-Q$ used in the calculations of the phase shift in order to ensure the convergence of the integrals and charge neutrality. Being its position entirely arbitrary, it can be easily ascertained that when it is put at very large distances, its effect is neutralized by its twin image and that the role of neutralizing charge is taken over by the twin image. Nonetheless, the compensating charge with its twin image can still be useful to mimic the effect of extra charges present on the support material in order to simulate more realistic boundary conditions, e.g. charge present in the tip.

Therefore, in order to simulate the effect of the PRW, the charge of the twin image induced by biprism was placed perpendicular to the biprism filament in simulation. In the vertical direction, the best fit using Eq. (3) for the charge is 140 e and the best fit using Eqs. (4),total-phase for the MIP is 5.5 V. The corresponding simulated phase image and equiphase contours of spacing $2\pi/8$ rad are shown in Figs. 2b and c. In the horizontal direction, the best fit for the charge is 150 e and the best fit for the MIP is 5.55 V. In both directions, different charge amount results in similar MIP values, suggesting that the MIP is not impacted significantly by this asymmetry. Fig. 2d shows the comparison of the phase profiles from the experiment and simulation in both vertical and horizontal directions. In order to simulate the effect of the boundary conditions, a total negative charge of −60 e was placed on the W tip (left of the sphere) with the result that MIP values remain unchanged.

In the following measurements, all the support materials (TEM grids) are conductive and grounded. We simulate the positive charge on polystyrene spheres by placing a single charge of the twin image perpendicular to the biprism, neglecting the small amount of negative charge on the supports. The electron-beam-induced charge on the sphere is corroborated by both analytical method Eq. (3) and the MI approach Eq. (9).

3. Results

Polystyrene spheres of different size were measured at temperatures of between 5.3 and 293 K using three specimen holders: a condenZero liquid-helium-cooled holder, a Gatan liquid-nitrogen-cooled holder and an FEI holder. In order to estimate measurement errors, the phase shift was analyzed in directions both parallel and perpendicular to the biprism. These errors may arise from differences between the holders and TEM grids, as well as environmental perturbations. The size of each

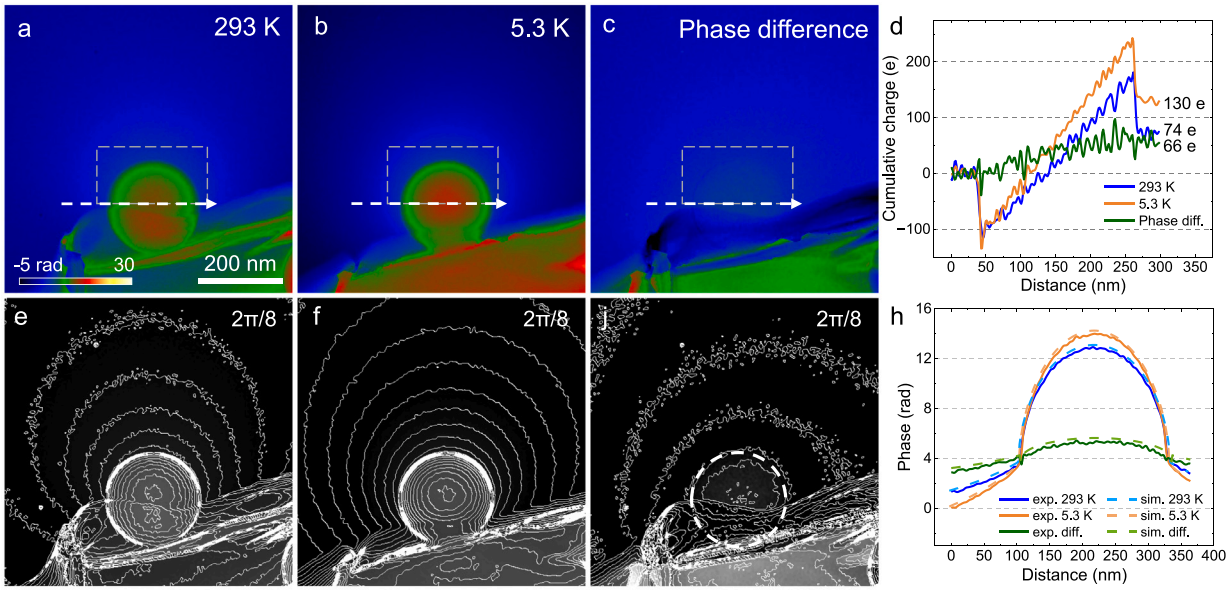

Fig. 3. Electron-beam-induced charging and MIP at 5.3 K. (a) Unwrapped phase image of a polystyrene sphere of diameter 230 nm recorded at 293 K. The sphere is attached to the edge of a carbon film. The gray dashed box marks a region that encloses slightly less than half of the sphere. The white dashed arrow marks the position used to extract a phase profile. (b) Phase image of the same polystyrene sphere recorded at 5.3 K. (c) Difference between (a) and (b). (d) Cumulative charge profiles obtained by applying a loop integral in the horizontal direction. The close-to-half-sized region of the polystyrene sphere has a total charge of 74 e at 293 K (blue line), 130 e at 5.3 K (orange) and 66 e as the residual (green). The linear charge profiles indicate surface charge distribution. (e–j) Equiphase contours of spacing $2\pi/8$ rad corresponding to (a), (b) and (c), respectively. (h) Phase profiles extracted along the white dashed arrows, with solid lines showing experimental results and dashed lines showing simulations. At 293 K, the best-fitting values of charge and MIP are 200 e and 5.50 V, respectively, whereas at 5.3 K they are 290 e and 6.10 V.

polystyrene sphere at each temperature was measured at multiple sample tilt angles to account for surface unevenness, providing an average value with a corresponding standard deviation. The polystyrene spheres were positioned on the edges of half-round conducting TEM grids, with the biprism aligned parallel to the straight edge of each grid.

3.1. MIP at reduced temperature

Figs. 3a–c show phase images of a 230-nm-diameter polystyrene sphere on a C film recorded at 293 K, 5.3 K and their difference, respectively. The recorded object and reference holograms are at actual magnification of 15 300× and pixel size of 0.3262 nm. The C film undergoes morphological changes as a result of the change in temperature. The dimensions and intensity scales of Figs. 3a and b have the same sizes and ranges, with the phase intensities aligned at the boundary of the sphere. The position of the polystyrene sphere is also aligned between the frames. Figs. 3e–j show corresponding equiphase contours of spacing $2\pi/8$ rad. The density of the contours reflects the phase gradient. A comparison of the equiphase lines at 293 and 5.3 K reveals that charge accumulation is higher at the lower temperature. In the phase difference image shown in Fig. 3j, the contours in the vacuum region above the dashed circle result from the excess charge. Within the dashed circle, the contours result from both excess charge and a change in the MIP of the polystyrene sphere. The cumulative charge in the gray dashed boxes (slightly smaller than a half sphere) in Figs. 3a–c is plotted in Fig. 3d, indicating that the amount of charge is 74 e at 293 K (blue line), 130 e at 5.3 K (orange line) and 66 e in the difference image (green line). The charge profiles at both temperatures again shows linear configuration, indicating mainly surface charge distribution. By using the methods described in Section 2.3 to Section 2.5, the corresponding phase shift of a charged polystyrene sphere was simulated for the different temperatures, including the contribution from the MIP.

Fig. 3h compares the phase profiles from the experiments (solid lines) and simulations (dashed lines) in the direction of the white dashed arrow. The phase shifts in the simulations outside the polystyrene sphere have same slopes as the solid experimental profiles, corresponding to amounts of charge of 200 e at 293 K and 280 e at 5.3 K. In the vertical direction, the charge amount is same as that deduced in horizontal direction. These values are approximately double those obtained from the half sphere MI approach, confirming that the different boundary condition represented by the grid does not introduce severe modifications in the charge distribution of the dielectric sphere. Knowing the contribution to the phase originating from electron-beam-induced charging, φ_Q, the contribution from the MIP could be deduced using Eq. (5). The simulated phase profiles in Fig. 3h are results of MIP 5.50 V at 293 K and 6.10 V at 5.3 K in horizontal directions. In vertical directions, they are 5.20 V at RT and 6.00 V at 5.3 K. In this way, the MIP values were determined to be (5.40 ± 0.17) V at 293 K and (6.07 ± 0.06) V at 5.3 K. The MIP at RT is consistent with the results shown in Fig. 1.

Fig. 4 shows phase images recorded at RT and 23 K from a different 230-nm-diameter polystyrene sphere. The recorded object and reference holograms are at actual magnification of 20 400× and pixel size of 0.2452 nm. The equiphase contours in Figs. 4a to e have a spacing of $2\pi/8$ rad. Similar to the results in Fig. 3, the phase shift and the density of the contours increase at lower temperature. The simulations in Figs. 4d and e show good agreement with the experimental results. Fig. 4f shows phase profiles from the experiments (solid lines) and simulations (dashed lines) along the white dashed arrows. By fitting the phase profiles in the left vacuum region, the amount of charge on the sphere was determined to be 200 e at 293 K and 320 e at 23 K. The cumulative charge profile at each temperature using MI approach, shown in Fig. S7 in Supplementary Material, is in a linear manner, indicating surface charge distribution. The corresponding MIP values were determined to be 5.90 V at 293 K and 6.73 V at 23 K. Based on the phase profile in the right vacuum region (5.80 V at 293 K, 6.70 V at 23 K) and the vertical direction (5.53 V at 293 K, 6.25 V at 23 K), the average MIP values were determined to be (5.74 ± 0.19) V at 293 K and (6.56 ± 0.27) V at 23 K. Details of the data and error treatment are given in Supplementary Material.

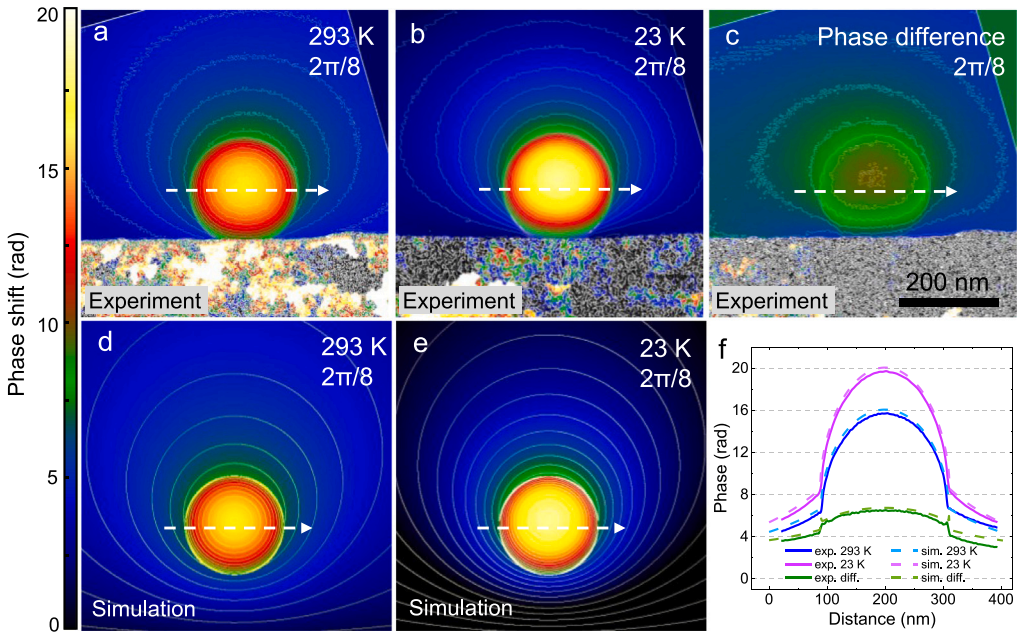

Fig. 4. Electron-beam-induced charging and MIP at 23 K. (a–c) Unwrapped phase images of a 230-nm-diameter polystyrene sphere attached to a Au grid, recorded at 293 K, 23 K and their difference. The equiphase contours have a spacing of $2\pi/8$ rad. (d, e) Simulated phase images at 293 and 23 K, respectively. The equiphase contours have a spacing of $2\pi/8$ rad. The intensity scale and lateral scale are normalized for all of the experimental and simulated phase images. (f) Phase profiles extracted along the white dashed arrows, with solid lines showing the experimental results and dashed lines the simulations. The dashed lines are shifted vertically by 0.3 rad relative to their experimental counterparts for clarity. The best-fitting values of MIP are 5.90 V at 293 K and 6.73 V at 23 K.

Other polystyrene spheres were studied to assess the influence of sphere size on the electron-beam-induced charge and the MIP. Figs. 5a–d show phase images recorded from a 430-nm-diameter polystyrene sphere attached to a 50-nm-thick Au film (visible in the lower left corner). The recorded object and reference holograms are at actual magnification of 20 400× and pixel size of 0.2452 nm. All of the phase images are shown with the same intensity and lateral scales, with the phase level aligned at the boundary of the polystyrene sphere. The faint superimposed stripes are equiphase contours of spacing $2\pi/4$ rad. A qualitative comparison between this larger polystyrene sphere and the previous smaller spheres reveals that the larger sphere has denser equiphase contours and accumulates more electron-beam-induced charge. In this case, the contours are influenced by the presence of two adjacent spheres, with the second sphere located at the lower right corner of the image. The equiphase contours and phase intensity do not change significantly with temperature, while the phase inside the sphere changes. This suggests that in this case the electron-beam-induced charge remains similar with temperature, but MIP is increased as temperature decreases.

Phase profiles extracted along the white dashed arrows at each temperature are shown in Figs. 5e and g, with solid lines representing experiments and dashed lines simulations. The polystyrene sphere at the lower right corner of the image affects the right part of the phase profile. Therefore, we focus on the left side of the vacuum region to determine the amount of charge using analytical simulations combined with the MI approach for a half-sphere. Fig. 5f shows magnified regions of the phase profiles from the left part of the vacuum region. The experimental (solid) and simulation (dashed) lines are shifted vertically by 0.3 rad for clarity. The simulated phase profiles correspond to charge amount of 470 e at 293 K, 370 e at 70 K and 420 e at 29 K. These results are consistent with the MI approach for a half-sphere, which yields 235 e at 293 K, 185 e at 70 K and 200 e at 29 K. The cumulative charge profile is shown in Fig. S8. The linear behavior indicates that the charge mainly distributes on the surface. Subsequently, the MIP values deduced in the direction of dashed arrows are 5.60 V at 293 K, 6.65 V at 70 K, 6.70 V at 29 K, and in vertical direction 5.40 V at 293 K, 6.35 V at 70 K, 6.45 V at 29 K. These turn out the average MIP values of (5.50 ± 0.14) V at 293 K, (6.50 ± 0.21) V at 70 K and (6.58 ± 0.18) V at 29 K.

At the lowest temperature of 5.3 K, high-frequency small-amplitude oscillations in the sample disrupt the holographic interference fringes at the boundary between the vacuum and the sample. Even thought the exposure time of each hologram is down to 0.2 s, the interference fringes became blur and discontinuous at the sphere boundary, which is different from that shown in Fig. 1a inset. During phase reconstruction, such fringe discontinuity introduces artifacts on the phase, causing the reconstructed phase at the boundary to shift by integer multiples of π and resulting in an increase or decrease in phase intensity. This effect results in the sharp phase jumps observed in Fig. 5d from the polystyrene sphere to the vacuum. Fig. 5g shows a phase profile extracted along the white dashed arrow at 5.3 K, in which the solid experimental line jumps at the boundaries at 70 and 490 nm on the horizontal axis. The amount of phase jump can be determined by the comparing the phase profiles of experiment and simulation. The amount of charge was determined by fitting the phase decay in vacuum and using MI approach for a half sphere. The phase decay in vacuum corresponds to an amount of charge of 422 e, while the MI approach gives 211 e for the half sphere. In order to measure the MIP at 5.3 K, the phase profile in the polystyrene sphere from 80 to 480 nm on the horizontal axis was fitted, resulting in a value for the MIP of (6.60 ± 0.13) V. Fig. 5h shows magnified versions of the regions marked in Fig. 5g. The upper inset shows the simulated (orange dashed) phase profile shifted by 0.3 rad vertically relative to the experimental (orange solid) profile for clarity. In the lower inset, the phase at the vacuum-polystyrene boundary is 2.12 rad for the experimental profile and −3.74 rad for the simulation, as marked by a black vertical line. The phase difference of 5.86 radian (2.12 + 3.74 rad), in combination with the 0.3 rad shift, corresponds to a total missing phase of approximately 2π rad.

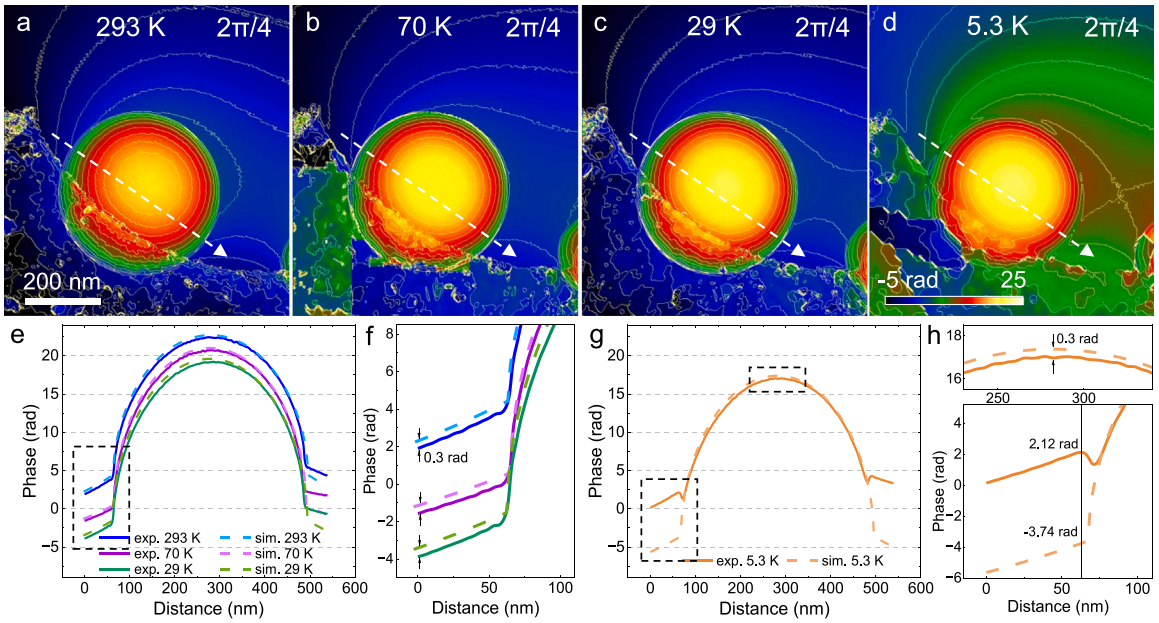

Fig. 5. Electron-beam-induced charging and MIP of a larger polystyrene sphere at cooling temperatures. (a–d) Unwrapped phase images of a 430-nm-diameter polystyrene sphere attached to a 50-nm-thick Au film (lower left corner) recorded at 293, 70, 29 and 5.3 K, respectively, with superimposed equiphase contours of spacing $2\pi/4$ rad. The details of the equiphase contours result from the presence of two closely-adjacent spheres with the same sign of charge. The other sphere is at the lower right corner. The intensity scales are normalized to the same range. (e) Phase profiles extracted along the white dashed arrows in (a) to (c). The simulation profiles (dashed lines) are shifted vertically by 0.3 rad relative to the experimental profiles (solid lines) for clarity. The MIP values used in the simulations are 5.60 V at 293 K, 6.65 V at 70 K and 6.70 V at 29 K. (f) Magnified region of the phase profiles on the left side, showing the consistency between the simulations and experiments and the 0.3 radian vertical shift. (g) Phase profile at 5.3 K. The phase jumps at ~ 70 nm and 500 nm on the horizontal axis result from interruption of the interference fringes at the vacuum-polystyrene boundary. The dashed line corresponds to a MIP of 6.69 V at 5.3 K. (h) Magnified regions of the phase profile on the upper and left sides. Based on the simulated phase profile, the missing phase at the boundary is $\approx 2\pi$ rad.

3.2. Temperature dependence

The relatively large spread of the MIP values reported in the literature makes an in-depth experimental research necessary in order to obtain a more reliable value.

Over 20 measurements were performed at different temperatures from polystyrene spheres with different diameters (230, 430 and 600 nm). Most of the data were recorded at temperatures of 293 and 5.3 K. Measurements made while returning to RT after cooling are also included. The electron-beam-induced charge amount at each temperature is firstly determined. From the phase images, it has shown that the electron-beam-induced charge does not exhibits clear dependence on temperature. For example, in Figs. 3 and 4, electron-beam-induced charge increases at lower temperature, while in Fig. 5 it does not change significantly. Additionally, the polystyrene sphere in Figs. 3 is supported by amorphous carbon film, while in Figs. 4 and 5 they are touching Au grid. It shows that the supporting materials have no obvious impact on electron-beam-induced charge on polystyrene spheres.

In order to visualize the relationship between charge and temperature among different sizes of polystyrene sphere and different supporting materials, the uniform surface charge density is considered. Fig. 6 shows the relationship between surface charge density and temperature, where the RT data include measurements taken after returning from cooling temperatures (red dot). Each data point is calculated upon the specific polystyrene sphere size at its corresponding temperature. Comparing the data at RT and back-to-RT, the charge and charge density slightly decreases after cooling cycle. The reduction of electron-beam-induced charge after temperature changing was also observed in the study of electron-beam-induced charging on Al_2O_3 apex [38], which is possibly due to conductive contamination deposited on the surface of the sample. The electron-beam-induced surface charge density is approximately independent of temperature, yielding an intercept value of about 9×10^8 e/cm^2 from linear fitting (blue dashed line). This would suggest the schottky barrier between the supporting substrate and sphere rarely changes as temperature. The schottky barrier is the difference between work function of metallic substrate (Au 5.45 eV at RT [39]) and electron affinity of the insulate sphere (polystyrene 0.4 eV at RT [40]), resulting in a barrier of 5.05 eV. The temperature dependence of work function of metals is approximately on the scale of 10^{-5} to 10^{-4} eV/K [41–43], and the temperature dependence of band gap of polymer is around on the scale of -10^{-3} eV/K [44]. At low temperatures, the Schottky barrier decreases by at most 0.32 eV, still maintaining a large barrier height.

The mean value of MIP is determined to be (5.55 ± 0.07) V at 293 K and (6.48 ± 0.24) V at 5.3 K, corresponding to an increase of 16.8% ± 4.2%. In addition to the effect of the PRW, the spread in the results at same temperatures originates from different external factors, including differences between the analysis methods, the use of different specimen holders and grids and environmental perturbations. In order to account for variations in MIP at the same temperature, weighted mean values were calculated by accounting for errors in the individual data. The treatment of errors is described in Supplementary Material Sec. 4.

Fig. 7 shows a plot of the relationship between temperature and MIP. The red point indicate the MIP measured after the cooling process returning to RT, which is nearly same as that at initial RT, demonstrating the reversibility of MIP cycling. The MIP values decrease with increasing temperature. The data were fitted to a linear function in the form of

$$V_{\mathrm{MIP}} = (6.60 \pm 0.07) - (2.92 \pm 0.54) \times 10^{-3} \cdot T, \tag{10}$$

shown as a blue solid line.

The linear approximation of MIP as temperature is achieved by mixing all the data with different sphere size, diameter from ~ 200 to

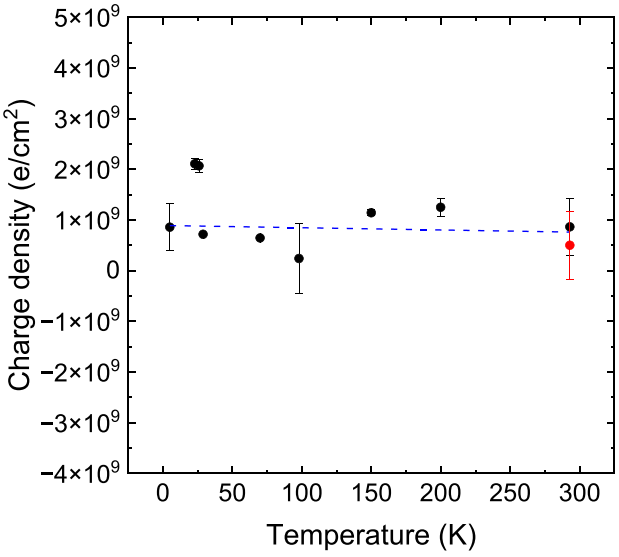

Fig. 6. Relationship between surface charge density and temperature. Black dots are results from RT to 5.3 K, with a linear fitting indicated by blue dashed line. The red dot refers to the measurements returning to RT again.

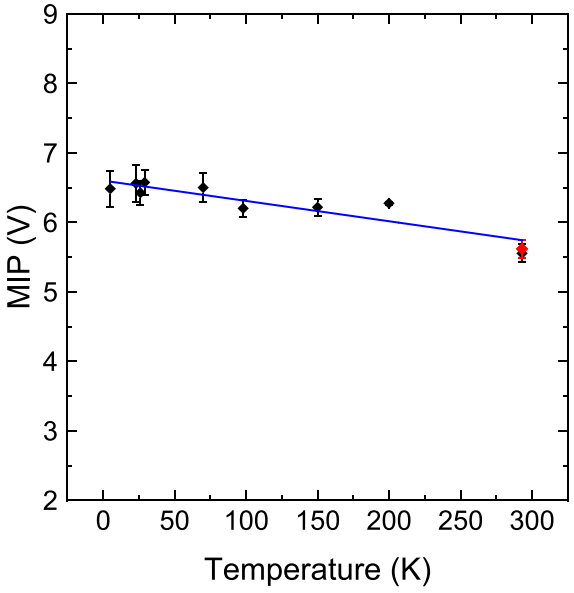

Fig. 7. Relationship between measured MIP and temperature is illustrated with diamond symbols for different sizes of polystyrene spheres. The red dot refers to the MIP at after returning to RT. The blue solid line is the linear fit to the data points except the red one.

~ 600 nm. It has been reported that MIP increases substantially when the size of nanoparticle decreases below 5 nm [20] and the thickness of film below 8 nm [27]. For larger size, the MIP does not change notably as size. Therefore, for the dimension on the order of a few hundred nanometers, the influence of size effect on MIP is negligible.

The linear relationship between MIP and temperature is corresponding to the proportional behavior between diamagnetic susceptibility and MIP measured on bulk polystyrene, which is provided in Supplementary Material Sec. 5.

4. Discussion

4.1. Different methods of MIP measurements

Polystyrene spheres are an excellent specimen to investigate by means of electron holography the effect of the long range electromagnetic field associated to their charging up [37,45], as well as to assess the performance of new techniques. In fact, the agreement of the MIP measurement with previously obtained values is often considered an additional validation of the method itself.

Fig. 8 plots the MIP of polystyrene sphere at RT measured by various methods. An earlier study using off-axis electron holography gave an average value of (8.5 ± 0.7) V for a sphere diameter of below 40 nm [26], where specimen charging was not observed or considered, likely due to limited phase resolution. Another off-axis electron holography study [24], using analytical method to fitting the phase profile, which is similar to current study, obtained the value of 6.1 V for the MIP of a ~200-nm sphere, assuming a volume charge distribution. Additionally, the compensating charge used in that work [24] is regarded as a shell surrounding the charged sphere. For in-line electron holography, the MIP of polystyrene became 8.2 and 8.4 V. Such an increase could be caused by the absence of phase shift due to charge on the sphere and by the worse resolution of small frequencies and very low spatial frequency information associated to the different reconstruction procedures.

Ptychography studies indicate the MIP of polystyrene sphere as (7.9 ± 0.64) V [46] and (8.43 ± 0.93) V [47], where MIP is also obtained by fitting the phase profile through the sphere center. However, the fitting is applied on the data between 20 to 80% of the sphere's radius. The smaller range of fitting area might induce an overestimated MIP value. A holographic tomography study [48] reconstructs 3D electrostatic potential, even the potential of small particles on the surface of polystyrene sphere. It shows a result of (8.4 ± 0.5) V by a potential profile through the sphere. No electron-beam-induced charge was observed or taken into account in most of the above studies.

The difference between these values may result from the difference in sphere size (i.e., a difference in the proportion of surface atoms [20]), different mass densities, different electron beam damage effects, errors in measurements of sphere size or an incorrect treatment of electron-beam-induced charging effects [26].

In the present study, several methodological improvements have been implemented, including the use of higher accelerating voltage of 300 kV, higher coherence of the electron beam, a Lorentz lens that provides a larger FOV and a 4K direct detection camera. By optimizing the magnification and exposure time, the fringe contrast reaches 30% to 55%, facilitating the separation of the MIP contribution to the electrostatic potential from the effects of electron-beam-induced specimen charging. If it were assumed that all the projected electrostatic potential originated from the MIP and the effects of electron-beam-induced charging were ignored, then the estimated MIP at RT would be approximately 7 V. This value is reasonably consistent with earlier studies.

4.2. Effect of charge distribution on MIP

It has been studied [30] that a pure surface-charge sphere assuming a relative permittivity, ϵ_r, of 100 possesses a linear profile on cumulative charge, while a pure volume-charge sphere with relative permittivity of 1 obtains curved profile. This comparison is also shown in Fig. S5. The relative permittivity of polystyrene is around 2.2 to 2.8 [49,50]. As long as $\epsilon_r > 1$, the charge distribution significantly increases on the surface, even though a small amount of charge is located in the bulk nearly homogeneous [30].

The electrostatic potential and the projected phase of a surface-charge sphere is different from the volume counterpart. For a 226-nm-diameter sphere distributed charge of 200 e, the projected phase at the center is 15.44 rad for surface charge and 16.69 rad for volume charge,

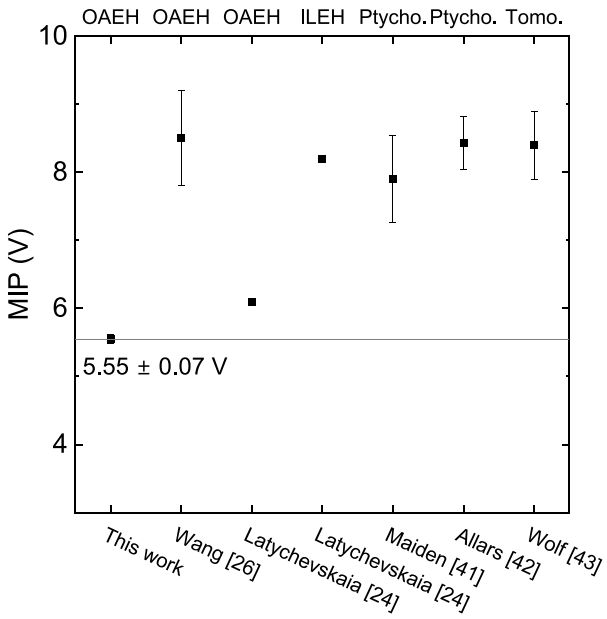

Fig. 8. Summary of MIP of polystyrene using different methods from literature. The gray horiozntal line marks the MIP in this work. OAEH and ILEH indicate off-axis and in-line electron-holography, respectively. Ptychography is shortened by Ptycho. and holographic tomoraphy is shortened by Tomo.

and the phase profiles differ only at the central area (Fig. S1). The MIP of the polystyrene sphere in Fig. 1 was determined as 5.5 V with the consideration of constant surface charge distribution. However, if constant volume charge distribution is applied, the MIP will be 4.85 V, which is ~12% smaller. Additionally, the phase profile of simulated volume-charge sphere is not consistent with the experimental data. In contrast, our data are consistent with surface charge distribution (Fig. S3).

Instead of free charge transfer between support-polystyrene contact, the compensating charge on the support does have impact on the charge distribution on the polystyrene sphere. Ideally, if the charge is perfectly uniformly distributed on the surface, the equiphase lines should be concentric circles symmetrical about the center of polystyrene sphere. However, the equiphase lines inside the sphere in all cases shift slightly away from the supports, resulting from the compensating negative charge on the supports. The convergent equiphase lines at the contacting interface also indicate opposite charge signs existing. Cumulative charge profiles shown in Figs. 1e and 3d indicate uniform surface charge density of half spheres by the linear feature on the direction parallel the contracting interface. Additionally, the cumulative charge on the vertical direction also presents linear profiles, which is shown in Figs. S7c (corresponding to Fig. 4) and S8e (corresponding to Fig. 5). Except for MI approach to obtain charge amount, the analytical method by fitting phase decay in the vacuum is done at different directions surrounding the sphere, giving an reasonable range [51]. The good consistence between the two methods indicate that the unevenness of charge distribute can be ignored. The accurate determination of the charge amount ensures that the subsequent MIP calculation is not subject to significant errors.

4.3. Change in mass density and electron scattering factor

Values of MIP of crystalline materials can be calculated theoretically from the electron scattering factors of isolated neutral atoms and the unit cell volume or density by using the equation [52,53]

$$V_{\mathrm{MIP}} = \frac{\hbar^2}{2\pi m e \Omega} \sum_i f_e^i(0), \tag{11}$$

where $\hbar$ is Planck's constant, m is the electron mass, e is the electron charge, Ω is the unit cell volume and $f_e^i(0)$ is the electron scattering factor at zero angle for each atom i in the unit cell volume. Both mass density ($1/\Omega$) and electron scattering factor may change when isolated atoms come closer together at lower temperature [11], resulting in a change in MIP.

In the first case, an increase in temperature corresponds to an increase in the interatomic distance, which is approximately linear at room temperature, but may become nonlinear at lower temperature and instead exhibit a plateau. This behavior may explain similarity of the MIP values measured at 5 K and 23 - 29 K.

More precisely, the mass density at RT is a function of the temperature, with its first derivative with respect to temperature corresponding to its coefficient of volume thermal expansion (β). Between a certain temperature range, for polystyrene film, the coefficient of thermal expansion (CTE) is nearly constant, and increases as increasing temperature [54–57]. The value of β is approximately (170 - 240) $\times$ 10^{-6} /K, which is almost three times the coefficient of linear thermal expansion (α) of (70 - 85) $\times$ 10^{-6} /K near RT [54–57].

Changes in volume (ΔV) and radius (Δr) with temperature (ΔT) can be written in the form $\Delta V = \beta V \Delta T$ and $\Delta r = \alpha r \Delta T$, respectively. Assuming α and β remain constant with temperature, extrapolation of the linear relationships towards lower temperatures suggests that the volume reduction for a 230-nm-diameter polystyrene sphere from 293 to 5 K is 3.8 $\times$ 10^5 nm^3 (6%), while the reduction in radius is 2.4 nm (2%). In practice, the experimental data indicate smaller reductions. For instance, in Fig. 3, the sphere radius is measured to decrease by 0.7% from 298 to 5.3 K, while in Fig. 5 the sphere radius decreases by 1%. This lower measured values may result from a change in the CTE with temperature [57,58] corresponding to the limited validity of the linear approximation at room temperature.

In the second case, the effect of the temperature on the electron scattering factor is more subtle, being related to the vibrations of the atoms around their equilibrium positions. In a real crystal, the effective electron scattering factor equals that of an isolating atom multiplied by a Debye–Waller factor. It has been reported that the Debye–Waller factor increases as temperature decreasing [53].

The former general considerations can be also extended to the amorphous case, and are suggesting that the main factor influencing the temperature dependence could be represented by the electron scattering factor, as the change in volume is negligible at the lower temperatures.

5. Conclusions

Off-axis electron holography has been used to measure the MIP of polystyrene spheres with diameters of between ~230 and ~600 nm over a temperature range from RTdown to 5.3 K, and to quantify electron-beam-induced charging effects. The high quality of experimental data, together with a systematic statistical analysis upon over 20 measurements, allows for an improved quantification of the electron-beam-induced charge and mean inner potential at each temperature.

The polystyrene spheres are observed to charge positively as a result of electron-beam-induced secondary electron emission, with larger particles supporting more charge. The amount of charge on each sphere is quantified using a combination of a model-independent and an analytical approach. The linear behavior of cumulative charge profile indicates that electron-beam-induced charge is mainly distributed on the surface instead of in the bulk. The surface charge density is approximately 9×10^8 e/cm^2.

The MIP is measured to be (5.55 ± 0.07) V at room temperature. It is found to increase steadily as the sample temperature is decreased, reaching a value of (6.48 ± 0.24) V at 5.3 K, corresponding to an increase of 16.8% ± 4.2% from the RTvalue. This behavior might be related to the increase in electron scattering factor through Debye–Waller factor as temperature decreasing, given that the sphere diameter does

not change significantly. To elucidate the direct physical mechanism of the change in electrostatic potential, more dedicated quantitative experiments may provide valuable insights, for example time-resolved electron holography to investigate the charge accumulation procedure and low dose study of secondary electron emission.

CRediT authorship contribution statement

Yan Lu: Writing – review & editing, Writing – original draft, Methodology, Investigation, Data curation, Conceptualization. **Peng-Han Lu:** Methodology, Investigation. **Fengshan Zheng:** Writing – review & editing, Methodology. **Dominik Biscette:** Methodology. **Denys Sutter:** Methodology. **Johan Chang:** Methodology. **Giulio Pozzi:** Writing – review & editing, Methodology, Investigation, Conceptualization. **Rafal E. Dunin-Borkowski:** Writing – review & editing, Supervision, Methodology, Funding acquisition, Conceptualization.

Declaration of competing interest

The authors declare that they have no known competing financial interests or personal relationships that could have appeared to influence the work reported in this paper.

Acknowledgments

This work was supported by the European Union as part of the HORIZON-INFRA-2021-SERV-01-04 project "Recyclable materials development at analytical research infrastructures" (ReMade@ARI) under grant agreement number 101058414 and co-funded by UK Research and Innovation (UKRI) under the UK government's Horizon Europe funding guarantee (grant number 10039728) and by the Swiss State Secretariat for Education, Research and Innovation (SERI) under contract number 22.00187.

Appendix A. Supplementary data

Supplementary material related to this article can be found online at https://doi.org/10.1016/j.ultramic.2026.114409.

Data availability

Data will be made available on request.

References

[1] J.C.H. Spence, On the accurate measurement of structure-factor amplitudes and phases by electron diffraction, Acta Crystallogr. Sect. A 49 (1993) 231–260.
[2] M. Gajdardziska-Josifovska, M.R. McCartney, W.J. De Ruijter, D.J Smith, J.K. Weiss, J.M. Zuo, Accurate measurements of mean inner potential of crystal wedges using digital electron holograms, Ultramicroscopy 50 (1993) 285–299.
[3] H. Bethe, Theorie der beugung von elektronen an kristallen, Ann. Phys., Lpz. 392 (1928) 55–129.
[4] P.A. Doyle, P.S. Turner, Relativistic Hartree–Fock X-ray and electron scattering factors, Acta Crystallogr. Sect. A: Cryst. Phys. Diffr. Theor. Gen. Crystallogr. 24 (1968) 390–397.
[5] A. Sanchez, M.A. Ochando, Calculation of the mean inner potential, J. Phys. C: Solid State Phys. 18 (1985) 33.
[6] P. Kruse, M. Schowalter, D. Lamoen, A. Rosenauer, D. Gerthsen, Determination of the mean inner potential in III–V semiconductors, Si and Ge by density functional theory and electron holography, Ultramicroscopy 106 (2006) 105–113.
[7] R.S. Pennington, C.B. Boothroyd, R.E. Dunin-Borkowski, Surface effects on mean inner potentials studied using density functional theory, Ultramicroscopy 159 (2015) 34–45.
[8] M. Schowalter, J.T. Titantah, D. Lamoen, P. Kruse, Ab initio computation of the mean inner Coulomb potential of amorphous carbon structures, Appl. Phys. Lett. 86 (2005) 112102.
[9] M. Schowalter, A. Rosenauer, D. Lamoen, P. Kruse, D. Gerthsen, Ab initio computation of the mean inner Coulomb potential of wurtzite-type semiconductors and gold, Appl. Phys. Lett. 88 (2006) 232108.
[10] S.M. Kathmann, I.-F.W. Kuo, C.J. Mundy, G.K. Schenter, Understanding the surface potential of water, J. Phys. Chem. B 115 (2011) 4369–4377.
[11] B. Sellner, S.M. Kathmann, A matter of quantum voltages, J. Chem. Phys. 141 (2014) 18C534.
[12] D. Gabor, A new microscopic principle, Nature 161 (1948) 777–778.
[13] G. Möllenstedt, H. Düker, Beobachtungen und messungen an biprisma-interferenzen mit elektronenwellen, Z. Phys. 145 (1956) 377–397.
[14] P.A. Midgley, An introduction to off-axis electron holography, Micron 32 (2001) 167–184.
[15] M. Lehmann, H. Lichte, Tutorial on off-axis electron holography, Microsc. Microanal. 8 (2002) 447–466.
[16] R.E. Dunin-Borkowski, T. Kasama, A. Wei, S.L. Tripp, M.J. Hÿtch, E. Snoeck, R.J. Harrison, A. Putnis, Off-axis electron holography of magnetic nanowires and chains, rings, and planar arrays of magnetic nanoparticles, Microsc. Res. Tech. 64 (2004) 390–402.
[17] H. Lichte, M. Lehmann, Electron holography—basics and applications, Rep. Progr. Phys. 71 (2007) 016102.
[18] G. Pozzi, M. Beleggia, T. Kasama, R.E. Dunin-Borkowski, Interferometric methods for mapping static electric and magnetic fields, C. R. Phys. 15 (2014) 126–139.
[19] J. Li, M.R. McCartney, R.E. Dunin-Borkowski, D.J. Smith, Determination of mean inner potential of germanium using off-axis electron holography, Acta Crystallogr. Sect. A 55 (1999) 652–658.
[20] R. Popescu, E. Müller, M. Wanner, D. Gerthsen, M. Schowalter, A. Rosenauer, A. Böttcher, D. Löffler, P. Weis, Increase of the mean inner Coulomb potential in Au clusters induced by surface tension and its implication for electron scattering, Phys. Rev. B: Condens. Matter Mater. Phys. 76 (2007) 235411.
[21] A. Auslender, G. Levi, V. Ezersky, S. Gorfman, O. Diéguez, A. Kohn, Mean inner potential of graphite measured by electron holography: Probing charge distribution and orbital diamagnetic susceptibility, Carbon 179 (2021) 288–298.
[22] F. Winkler, A.H. Tavabi, J. Barthel, M. Duchamp, E. Yucelen, S. Borghardt, B.E. Kardynal, R.E. Dunin-Borkowski, Quantitative measurement of mean inner potential and specimen thickness from high-resolution off-axis electron holograms of ultra-thin layered WSe_2, Ultramicroscopy 178 (2017) 38–47.
[23] M.N. Yesibolati, S. Laganà, H. Sun, M. Beleggia, S.M. Kathmann, T. Kasama, K. Mølhave, Mean inner potential of liquid water, Phys. Rev. Lett. 124 (2020) 065502.
[24] T. Latychevskaia, P. Formanek, C.T. Koch, A. Lubk, Off-axis and inline electron holography: Experimental comparison, Ultramicroscopy 110 (2010) 472–482.
[25] Y.C. Wang, T.M. Chou, M. Libera, T.F. Kelly, Transmission electron holography of silicon nanospheres with surface oxide layers, Appl. Phys. Lett. 70 (1997) 1296–1298.
[26] Y.C. Wang, T.M. Chou, M. Libera, E. Voelkl, B.G. Frost, Measurement of polystyrene mean inner potential by transmission electron holography of latex spheres, Microsc. Microanal. 4 (1998) 146–157.
[27] M. Wanner, D. Bach, D. Gerthsen, R. Werner, B. Tesche, Electron holography of thin amorphous carbon films: Measurement of the mean inner potential and a thickness-independent phase shift, Ultramicroscopy 106 (2006) 341–345.
[28] M. Beleggia, T. Kasama, R.E. Dunin-Borkowski, S. Hofmann, G. Pozzi, Direct measurement of the charge distribution along a biased carbon nanotube bundle using electron holography, Appl. Phys. Lett. 98 (2011) 243101.
[29] C. Gatel, A. Lubk, G. Pozzi, E. Snoeck, M. Hÿtch, Counting elementary charges on nanoparticles by electron holography, Phys. Rev. Lett. 111 (2013) 025501.
[30] M. Beleggia, L.C. Gontard, R.E. Dunin-Borkowski, Local charge measurement using off-axis electron holography, J. Phys. D: Appl. Phys. 49 (2016) 294003.
[31] F. Zheng, J. Caron, V. Migunov, M. Beleggia, G. Pozzi, R.E. Dunin-Borkowski, Measurement of charge density in nanoscale materials using off-axis electron holography, J. Electron Spectrosc. Relat. Phenom. 241 (2020) 146881.
[32] K. Siangchaew, M. Libera, The influence of fast secondary electrons on the aromatic structure of polystyrene, Phil. Mag. A 80 (2000) 1001–1016.
[33] E. Voelkl, D. Tang, Approaching routine $2\pi/1000$ phase resolution for off-axis type holography, Ultramicroscopy 110 (2010) 447–459.
[34] G. Matteucci, G. Missiroli, E. Nichelatti, A. Migliori, M. Vanzi, G. Pozzi, Electron holography of long-range electric and magnetic fields, J. Appl. Phys. 69 (1991) 1835–1842.
[35] C.J. Russo, R. Henderson, Charge accumulation in electron cryomicroscopy, Ultramicroscopy 187 (2018) 43–49.
[36] H. Tomozawa, D. Braun, S.D. Phillips, R. Worland, A.J. Heeger, H. Kroemer, Metal-polymer schottky barriers on processible polymers, Synth. Met. 28 (1989) 687–690.
[37] G. Matteucci, G.F. Missiroli, G. Pozzi, Electron holography of long-range electrostatic fields, Adv. Imaging Electron Phys. 122 (2002) 173–249.
[38] F. Zheng, M. Beleggia, V. Migunov, G. Pozzi, R.E. Dunin-Borkowski, Electron-beam-induced charging of an Al_2O_3 nanotip studied using off-axis electron holography, Ultramicroscopy 241 (2022) 113593.
[39] W.M.H. Sachtler, G.J.H. Dorgelo, A.A. Holscher, The work function of gold, Surf. Sci. 5 (1966) 221–229.
[40] N. Ueno, K. Sugita, K. Seki, H. Inokuchi, Electron affinities of polystyrene and poly (2-vinylpyridine) by low-energy electron inelastic scattering, Japan. J. Appl. Phys. 24 (1985) 1156.

[41] H. Kawano, T. Kenpō, Y. Hidaka, A new and simple method to determine the temperature coefficient of effective work function for thermal positive ion production on a clean polycrystalline metal surface, Int. J. Mass Spectrom. Ion Process. 67 (1985) 137–145.
[42] A. Kiejna, On the temperature dependence of the work function, Surf. Sci. 178 (1986) 349–358.
[43] S. Seely, Work function and temperature, Phys. Rev. 59 (1941) 75.
[44] F. Yakuphanoglu, M. Arslan, M. Küçükislamoğlu, M. Zengin, Temperature dependence of the optical band gap and refractive index of poly (ethylene terepthalate) oligomer–DDQ complex thin film, Sol. Energy 79 (2005) 96–100.
[45] J. Komrska, Scalar diffraction theory in electron optics, in: L. Marton (Ed.), in: Advances in Electronics and Electron Physics, vol. 30, Academic Press, 1971, pp. 139–234.
[46] A.M. Maiden, M.C. Sarahan, M.D. Stagg, S.M. Schramm, M.J. Humphry, Quantitative electron phase imaging with high sensitivity and an unlimited field of view, Sci. Rep. 5 (2015) 14690.
[47] F. Allars, P.H. Lu, M. Kruth, R.E. Dunin-Borkowski, J.M. Rodenburg, A.M. Maiden, Efficient large field of view electron phase imaging using near-field electron ptychography with a diffuser, Ultramicroscopy 231 (2021) 113257.
[48] D. Wolf, A. Lubk, H. Lichte, Weighted simultaneous iterative reconstruction technique for single-axis tomography, Ultramicroscopy 136 (2014) 15–25.
[49] S. Zhang, Y. Zhang, Z.Y. Wang, W. Qiao, Synthesis and characterizations of polystyrene materials with low dielectric constant and low dielectric loss at high frequency, J. Appl. Polym. Sci. 140 (2023) e54012.
[50] M. Dai, J. Sun, Q. Fang, A fluorinated cross-linked polystyrene with good dielectric properties at high frequency derived from bio-based vanillin, Polyer Chem. 13 (2022) 4484–4489.
[51] Y. Lu, F. Zheng, Q. Lan, M. Schnedler, P. Ebert, R.E. Dunin-Borkowski, Counting point defects at nanoparticle surfaces by electron holography, Nano Lett. 22 (2022) 6936–6941.
[52] J.A. Ibers, Atomic scattering amplitudes for electrons, Acta Crystallogr. 11 (1958) 178–183.
[53] L.M. Peng, Electron atomic scattering factors and scattering potentials of crystals, Micron 30 (1999) 625–648.
[54] W. Patnode, W.J. Scheiber, The density, thermal expansion, vapor pressure, and refractive index of styrene, and the density and thermal expansion of polystyrene, J. Am. Chem. Soc. 61 (1939) 3449–3451.
[55] P.S. Turner, Thermal-expansion stresses in reinforced plastics, J. Res. Natl. Bur. Stand. 37 (1946) 239–250.
[56] G. Beaucage, R. Composto, R.S. Stein, Ellipsometric study of the glass transition and thermal expansion coefficients of thin polymer films, J. Polym. Sci. Part B: Polym. Phys. 31 (1993) 319–326.
[57] Y. Shin, H. Lee, W. Lee, D.Y. Ryu, Glass transition and thermal expansion behavior of polystyrene films supported on polystyrene-grafted substrates, Macromolecules 49 (2016) 5291–5296.
[58] K.F. Rogers, L.N. Phillips, D.M. Kingston-Lee, B. Yates, M.J. Overy, J.P. Sargent, B.A. McCalla, The thermal expansion of carbon fibre-reinforced plastics: Part 1 the influence of fibre type and orientation, J. Mater. Sci. 12 (1977) 718–734.